PHYSICAL REVIEW B **106**, 064208 (2022)

Non-Hermitian many-body localization with open boundaries

Kuldeep Suthar,[1,*] Yi-Cheng Wang,[1,2] Yi-Ping Huang,[3,4] H. H. Jen,[1,5,†] and Jhih-Shih You[6,‡]
[1]*Institute of Atomic and Molecular Sciences, Academia Sinica, Taipei 10617, Taiwan*
[2]*Department of Physics, National Taiwan University, Taipei 10617, Taiwan*
[3]*Department of Physics, National Tsing Hua University, Hsinchu 300044, Taiwan*
[4]*Institute of Physics, Academia Sinica, Taipei 115, Taiwan*
[5]*Physics Division, National Center for Theoretical Sciences, Taipei 10617, Taiwan*
[6]*Department of Physics, National Taiwan Normal University, Taipei 11677, Taiwan*

(Received 5 April 2022; revised 18 July 2022; accepted 22 August 2022; published 31 August 2022)

The explorations of non-Hermiticity have been devoted to investigate the disorder-induced many-body localization (MBL). However, the sensitivity of the spatial boundary conditions and the interplay of the non-Hermitian skin effect with many-body phenomena are not yet clear. For a MBL system in the presence of nonreciprocal tunnelings and random disorder potential, we identify two different complex-real spectral transitions, one is present for both open and periodic boundaries while the other is present only for open boundaries of coupled non-Hermitian chains. The later is driven due to the interchain coupling at weak disorder where the level statistics of the real eigenenergy phase follows a Gaussian orthogonal ensemble. We further characterize wave functions through the (biorthogonal) inverse participation ratio and fractal dimension, which reveal the suppression of skin effect in the non-Hermitian MBL phase. Finally, we demonstrate that the quench dynamics of the local particle density, spin imbalance, and entanglement entropy also signify the hallmark of the boundary effects and nonergodic character of many-body localization.

DOI: 10.1103/PhysRevB.106.064208

I. INTRODUCTION

When traditional quantum mechanics postulates Hermiticity, numerous developments have been made for exploring non-Hermitian quantum mechanics in various fields of physics like condensed matter, cold atoms, and open quantum systems [1–6]. The recent experimental advances provide access to engineer the non-Hermitian Hamiltonians with the dissipation and nonreciprocal tunnelings [7–11]. These developments allow us to explore fundamental physics of localization. The interplay between disorder and non-Hermiticity due to asymmetric hopping was first investigated by the pioneering works of Hatano and Nelson, which reveal a real-complex transition of a single-particle spectrum [12–14]. Moreover, it has been shown that the random potential can suppress the complex eigenenergies of an interacting single Hatano-Nelson chain with periodic boundary condition (PBC) and the spectral transition is accompanied by non-Hermitian MBL transition [15]. Similar phenomena have also been found for quasiperiodic potential [16,17]. Since the disordered single-chain model respecting time-reversal symmetry belongs to the symmetry class AI, its localized phase follows the real Poisson ensemble while the delocalized phase follows the Ginibre ensemble [18–20].

The choice of the imposed boundary conditions plays a decisive role in determining the properties of non-Hermitian systems. One fascinating phenomenon that has no Hermitian counterparts is the non-Hermitian skin effect (NHSE). It describes the anomalous localization for an extensive number of bulk modes which can occur at the boundaries of non-Hermitian open lattices [21–31]. This effect fundamentally challenges our knowledge of the band theory and violates the conventional bulk boundary correspondence of Hermitian systems which connects robust edge states to bulk topological invariants. For non-Hermitian Hamiltonians, the understanding of NHSE in noninteracting systems relies on the non-Bloch theory in which non-Bloch topological invariants are defined in generalized Brillouin zones [6,32]. The NHSE has been realized in various experimental setups of photonics [7,33], electrical circuits [8,9,34], metamaterials [35,36], and ultracold atoms [10,11]. More recently, the fate of skin modes in fermionic and bosonic systems with many-body correlations has been investigated [37–47]. However, little is known about the robustness of NHSE on the localization properties of many-body disordered systems.

To date, the unusual characteristics of non-Hermitian systems have been explored from various perspectives. One of them is the sensitivity of boundary conditions which leads to the emergence of NHSE. Under PBC, for a single periodic non-Hermitian chain with nonreciprocal tunnelings, the many-body localization transition occurs with a complex-real spectral transition [15,16]. However, this does not apply to a single chain under open boundary condition (OBC) due to the real spectrum in the presence of NHSE. Recently, many theoretical studies have uncovered that the nontrivial behavior arises due to the finite coupling between two one-band subsystems with different generalized Brillouin zones [48–52]. It

---

[*] Corresponding author: kuldeep@gate.sinica.edu.tw

[†] Corresponding author: sappyjen@gmail.com

[‡] Corresponding author: jhihshihyou@ntnu.edu.tw

is legitimate to ask whether the boundary-induced phenomena exist when two subsystems are coupled together with unequal (or equal) nonreciprocal hopping parameters. The interplay of the nonreciprocal hoppings and coupling strength of two chains for a many-body disordered system is yet to be explored.

In this work we study the spectral statistics, eigenstate properties, and nonequilibrium dynamics of many-body coupled Hatano-Nelson chains in the presence of a random disorder potential. In particular, we investigate the role of the imposed boundary conditions on the characteristic properties of a non-Hermitian two-chain system. We identify a parameter space of interchain coupling and nonreciprocal tunneling parameters, where a complex-real spectral transition is observed for finite open chains, while the spectrum for PBC maintains complex. The spectral transition is accompanied by the change in nearest-level-spacing distribution of eigenenergies and an average complex spacing ratio. At weak disorder, the level statistics changes from Ginibre to Gaussian orthogonal ensemble (GOE), corresponding to the spectral transition as the interchain coupling increases. The system enters into the many-body localized phase with increases in disorder strength and this phase possesses a real eigenspectrum. Our work reports a spectral transition which is unique to the coupled fermionic chains and enhances the prospects of observing more spectral transitions as compared to its single-chain counterpart. We further confirm the MBL by eigenstate properties such as inverse participation ratio and fractal dimension, and show the suppression of NHSE in the localized phase. Finally, the boundary effects and signature of MBL are corroborated in the time evolution of imbalance and entanglement entropy.

This work is organized as follows. Section II introduces the interacting two-chain Hatano-Nelson model. In Sec. III we discuss the spectral transition in eigenspectrum, the level statistics, the inverse participation ratio, the quench dynamics of spin imbalance and entanglement entropy, and experimental realization of the model Hamiltonian. Finally, we summarize our results in Sec. IV.

II. THE MODEL

We consider two coupled non-Hermitian Hatano-Nelson chains of interacting fermions in the presence of a random potential. In the two-chain geometry, the two chains can be interpreted as two components of spin-1/2 fermions [see Fig. 1(a)]. The model Hamiltonian reads as

$$\begin{aligned}\hat{H} = &-\sum_{j,\sigma} J(e^{-g_\sigma}\hat{c}^\dagger_{j,\sigma}\hat{c}_{j+1,\sigma} + e^{g_\sigma}\hat{c}^\dagger_{j+1,\sigma}\hat{c}_{j,\sigma})\\ &-\sum_j (K\,\hat{c}^\dagger_{j,\uparrow}\hat{c}_{j,\downarrow} + \text{H.c.})\\ &+U\sum_j \hat{n}_{j,\uparrow}\hat{n}_{j,\downarrow} + \sum_{j,\sigma}\epsilon_{j\sigma}\hat{n}_{j,\sigma},\end{aligned} \tag{1}$$

where j and $\sigma = \{\uparrow, \downarrow\}$ represent the spatial and spin (chain) indices, J is the hopping strength between neighboring lattice sites on the same chain, g_σ is the non-Hermiticity parameter of σ spin, $\hat{c}^\dagger_{j,\sigma}$ ($\hat{c}_{j,\sigma}$) creates (annihilates) fermion with spin σ at jth site, $\hat{n}_{j,\sigma} = \hat{c}^\dagger_{j,\sigma}\hat{c}_{j,\sigma}$ is the occupation number operator, K is the interchain coupling strength, U is the on-site interaction strength, and $\epsilon_{j\sigma}$ is the random disorder potential chosen between $[-W, W]$ with W being the disorder strength. Here we primarily consider the uncorrelated (spin-dependent) disorder, which breaks SU(2) spin symmetry of the model and is known to induce full localization in the Hermitian system [53–56]. However, we also discuss the contrast behavior due to spin-independent disorder potential ($\epsilon_{j\uparrow} = \epsilon_{j\downarrow}$) for some specific cases. In the present work we set the hopping amplitude J as the unit of energy scale, $J = 1$. We consider a system of fermions at half-filling, i.e., the total number of fermions $N = N_\uparrow + N_\downarrow = L$ with L being the number of lattice sites along the ladder. It is also worth noting, according to the symmetry class of a non-Hermitian system [57–59], the model considered here belongs to the symmetry class AI that preserves the time-reversal symmetry ($H = H^*$) and breaks the transposition symmetry ($H \neq H^T$).

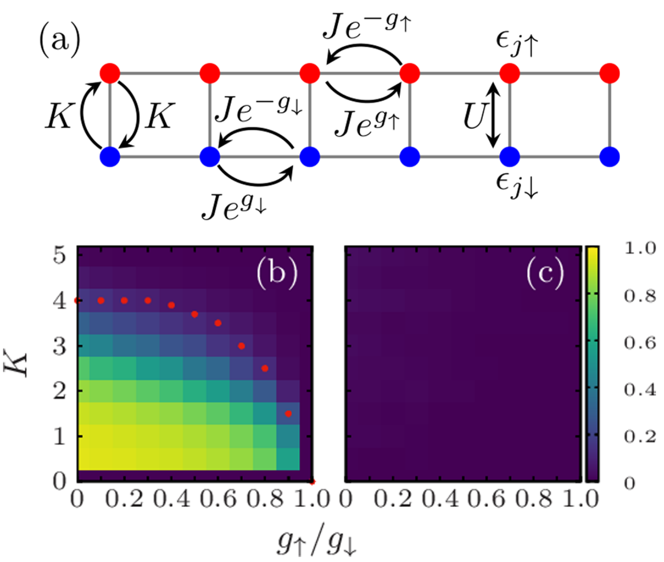

FIG. 1. (a) The schematic representation of a two-chain Hatano-Nelson model. (b) and (c) The complex energy fraction f_{im} in K-$g_\uparrow/g_\downarrow$ plane. Disorder-averaged eigenspectrum distributions of a finite lattice with $L = 7$ sites under open boundary conditions are shown for two representative cases. (b) $W = 2$ corresponds to the ergodic regime while (c) $W = 30$ represents the MBL regime. The yellow and blue colors represent the parameter space of the model with complex ($f_{\text{im}} = 1$) and real ($f_{\text{im}} = 0$) eigenenergies, respectively. The red circles in (b) represent the critical interchain coupling strength (K_c) of complex-real spectral transition for different $g_\uparrow/g_\downarrow$. The interplay of K and g_σ's results into (b) complex-real transitions at weak disorder and (c) at strong disorder the spectrum remains real. Here we fix $U = 1$ and set $J = 1$ as the unit of the energy. The spectrum is averaged over 200 disorder samples.

In non-Hermitian systems with nonreciprocal hoppings, the spectra are extremely sensitive to the boundary conditions. For the two-chain model with dissimilar non-Hermiticity parameters $g_\uparrow \neq g_\downarrow$, the interchain coupling K can further yield nontrivial interference between chains. When $K = 0$, the open boundary condition allows us to remove g_σ by an imaginary gauge transformation (IGT) [60], $c_{j,\sigma} \rightarrow e^{g_\sigma j}c_{j,\sigma}$ and $c^\dagger_{j,\sigma} \rightarrow e^{-g_\sigma j}c^\dagger_{j,\sigma}$. As a result, Eq. (1) becomes a Hermitian disordered Hubbard model and all the many-body eigenenergies are real under OBC. For any $K \neq 0$, if $g_\uparrow \neq g_\downarrow$, g_σ cannot be removed by such a transformation, and imaginary parts of eigenenergies could appear in the spectrum. While the complex (real) spectrum of the single Hatano-Nelson chain is unique to the PBC (OBC), much richer eigenspectrum and many-body dynamics arise from the two-chain model under OBC.

III. RESULTS AND DISCUSSIONS

A. Real-complex transition of eigenspectrum

We first discuss the characteristic properties of the change in the eigenspectrum as a function of the interchain coupling K and non-Hermiticity parameters g_σ. To manifest the complex spectrum, we define the fraction of the complex energies $f_{\text{im}} = \overline{D_{\text{im}}/D}$, where D_{im} is the number of complex eigenenergies with nonzero imaginary part, D is the total number of eigenenergies, and the overline denotes the disorder average. The eigenenergies are defined as complex if $|\text{Im}\{E\}| \geqslant C$ with a cut-off $C = 10^{-13}$, which is identified based on the machine error. Since the model Hamiltonian preserves the time-reversal symmetry, we find that the imaginary parts of the energies appear symmetric to the real axis (see Appendix A for details).

Under OBC we first show the disorder-averaged fraction of the complex energies for weak disorder strengths ($W = 2$) in Fig. 1(b). The phase diagram can be divided into various regimes (i) $K = 0 \rightarrow K \neq 0$, (ii) $g_\uparrow \neq g_\downarrow \rightarrow g_\uparrow = g_\downarrow$, and (iii) $K \gg 1$. (i) When tuning the interchain coupling from decoupled ($K = 0$) to the coupled ($K \neq 0$) limit, we numerically verify that the phase diagram, except for $g_\uparrow/g_\downarrow = 1$, exhibits a real-complex spectral transition of the many-body eigenenergies [52]. In the limit of weak interchain coupling ($K \approx 10^{-5}$), the energy spectrum of the system resembles that of two individual uncoupled chains. It is important to note that a single Hatano-Nelson chain under OBC possesses real spectrum, this is because the nonreciprocal hopping can be gauged out using IGT and a non-Hermitian Hamiltonian with real energies can be mapped to a Hermitian Hamiltonian. To elucidate the effect of nonzero K on the eigenenergy distribution, we first consider the $g_\uparrow = g_\downarrow$ case where the forward and backward hoppings are identical for both chains. In this scenario, the anomalous localization due to NHSE still survives and the validity of IGT makes the energy spectrum real. On the other hand, the $g_\uparrow \neq g_\downarrow$ case leads to dissimilar inverse skin lengths (of NHSE) for each of the chains. The effects of g_σ's cannot be removed through IGT for unequal non-Hermiticity parameters. The collective effects of the two different skin modes result into a complex eigenenergy phase [52]. Hence, as the interchain coupling is varied from a decoupled ($K = 0$) to the coupled ($K \neq 0$) limit, we numerically find that the phase diagram, except for $g_\uparrow/g_\downarrow = 1$, exhibits a real-complex spectral transition of the many-body eigenenergies. (ii) We further discuss the effects of $g_\uparrow/g_\downarrow$ on the eigenspectrum. A smooth complex-real spectral transition is observed as the ratio $g_\uparrow/g_\downarrow$ approaches unity. Note that the OBC eigenenergies are real at $g_\uparrow/g_\downarrow = 1$ because IGT is valid for this case. As the $g_\uparrow/g_\downarrow$ ratio increases, the critical interchain coupling strength (K_c) of the complex-real transition decreases, as evident in Fig. 1(b). For a hybridized coupled chains with $g_\uparrow = 0$ and $g_\downarrow \neq 0$ or vice versa, K_c reaches the maximum and for $g_\uparrow = g_\downarrow$, $K_c = 0$ as for the later case the system can be mapped to a Hermitian one. (iii) At sufficiently higher K, the effect of the non-Hermiticity is suppressed and the system possesses real spectra irrespective of any $g_\uparrow/g_\downarrow$. The quantitative variation of f_{im} for different system sizes is discussed in Appendix A, which confirms the robustness of the phase diagram with L.

At strong disorder strengths, the system is expected to be in the many-body localized phase. As shown in Fig. 1(c), the OBC eigenenergies remain real in the entire K-$g_\uparrow/g_\downarrow$ plane since the strong disorder potential destroys the non-Hermiticity. Hence, we find a disorder-induced complex-real transition. It is important to note that for the coupled-chain system this transition exists not only for OBC but also for PBC, in stark contrast to the occurrence of the interchain coupling driven transition which is sensitive to the boundary conditions. We have provided the details of the eigenspectrum with PBC in Appendix A.

B. Spectral statistics

We now investigate the level statistics to unveil the universal features of the eigenenergies. For non-Hermitian disordered systems with time-reversal symmetry, the localized phase follows the real Poisson ensemble while the delocalized phase follows the Ginibre ensemble [18–20]. The nearest-level-spacings for an eigenenergy E_i are defined as $|E_i - E_i^{\text{NN}}|$, where E_i^{NN} is an eigenvalue nearest to E_i in the complex energy plane. We first perform an unfolding of the spectrum to obtain the histogram of the Euclidean distance between nearest-neighbor eigenvalues [20,57]. Here the unfolding procedure is applied to both complex and real spectra of the model. To get the unfolding spectrum, we first compute the nearest-neighbour distance of the eigenvalues

$$d_{1,i} \equiv \min_j |E_i - E_j|. \tag{2}$$

Next, the local mean density of the eigenvalues is computed as

$$\bar{\rho}_i = \frac{n}{\pi d_{n,i}^2}, \tag{3}$$

where n is sufficiently larger than unity ($\approx$30), but very small compared to the Hamiltonian matrix size. Here $d_{n,i}$ is the nth nearest-neighbor distance from E_i. The rescaled nearest-neighbor distance s_i is obtained as

$$s_i = d_{1,i}\sqrt{\bar{\rho}_i}, \tag{4}$$

which removes the dependence of the local density of eigenvalues on the level-spacing. Finally, the statistics of nearest-neighbor spacings are computed from s_i.

At weak disorder, the complex energy spectrum with smaller K and $g_\uparrow \neq g_\downarrow$ obeys the Ginibre distribution $P_{\text{Gin}}^{\text{C}}(s) = cp(cs)$ which describes the ensemble of non-Hermitian Gaussian random matrices [20,57,61]. Here

$$p(s) = \lim_{N\to\infty}\left[\prod_{n=1}^{N-1} e_n(s^2)e^{-s^2}\right]\sum_{n=1}^{N-1}\frac{2s^{2n+1}}{n!\,e_n(s^2)}, \tag{5}$$

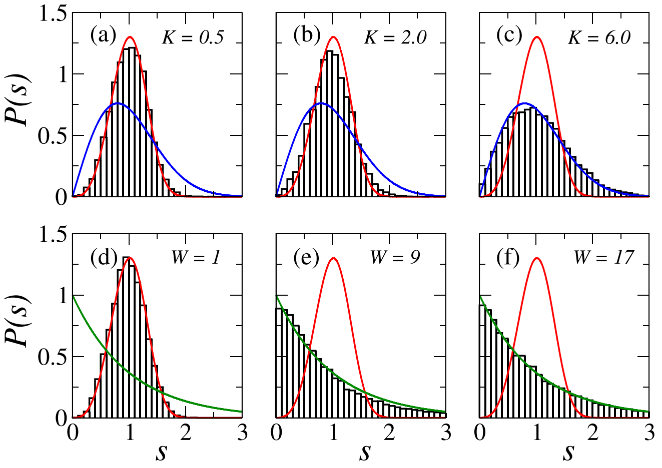

FIG. 2. (a)–(c) The unfolded nearest-level-spacing distributions with K at $W = 2$ and $g_\uparrow/g_\downarrow = 0.5$. At smaller K, the distribution follows Ginibre distribution and at larger K, it follows GOE distribution. (d)–(f) The level-spacing distributions as a function of the disorder strengths for $K = 1$ and $g_\uparrow/g_\downarrow = 0.5$. The disorder-driven complex-real transition corresponds to the Ginibre-to-Poisson level-spacing transition. The red, blue, and green lines represent the Ginibre, GOE, and (real) Poisson distributions, respectively. Here the system size $L = 8$, on-site interaction $U = 1$, and disorder average is performed for 100 realizations.

with $e_n(x) = \sum_{m=0}^{n} \frac{x^m}{m!}$ and $c = \int_0^\infty ds\, s\, p(s) = 1.1429$ [20,62]. We further find that for the strong interchain coupling K or equal g_σ's of two chains, the real eigenspectrum of a weak disorder case follows the level statistics of GOE. The level-spacing distribution of GOE is

$$P^{\mathrm{R}}_{\mathrm{GOE}}(s) = \frac{\pi s}{2} \exp(-\pi s^2/4). \tag{6}$$

The nearest-neighbor level-spacing distributions as a function of K at $W = 2$ are plotted in Figs. 2(a)–2(c). It shows that for smaller K, the distribution is a Ginibre distribution while at larger K, the system follows GOE distribution. Hence, the general features of the non-Hermitian Hamiltonian with purely real eigenvalues can be mapped to a Hermitian Hamiltonian. On the other hand, at strong disorder case, the localized phase with real eigenspectrum is characterized by the Poisson level distribution $P^{\mathrm{R}}_{\mathrm{Po}}(s) = \exp(-s)$. The level-spacing distribution as a function of W is illustrated in Figs. 2(d)–2(f), which suggests the MBL phase transition of two-chain Hatano-Nelson model.

We further study the complex level-spacing ratio [61]. The level-spacing ratio is a dimensionless complex variable $z_i \equiv [(E_i - E_i^{\mathrm{NN}})/(E_i - E_i^{\mathrm{NNN}})] \equiv r_i e^{i\theta_i}$ with the amplitude $r_i \equiv |z_i|$, which also allows us to extract the angular information. Here E_i^{NNN} is a next-nearest-neighbor eigenvalue to E_i. The mean level-spacing ratio $\langle r\rangle$ is obtained by the average of r_i over the energy window and number of disorder realizations. This definition is the generalization of the well-known gap ratio defined for Hermitian isolated quantum systems [63,64]. Here we consider the energy window to be 10% eigenvalues around the center of the eigenspectrum in the complex energy plane. This allows us to obtain a large number of eigenvalues for the level statistics and ascertain that their eigenstates share similar localization properties. The number of disorder realizations is chosen such that the total number of eigenvalues is $\sim 10^6$.

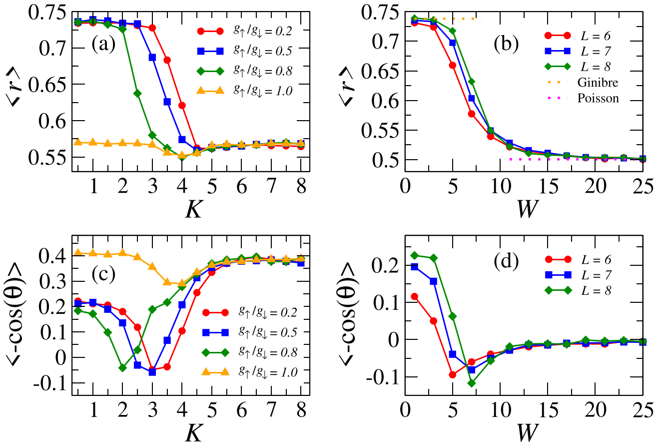

FIG. 3. The average level-spacing ratio $\langle r\rangle$ for the coupled Hatano-Nelson model exhibiting AI symmetry class. (a) Evolution of $\langle r\rangle$ as a function of K for different non-Hermiticity parameters at $W = 2$. As $g_\uparrow/g_\downarrow$ ratio increases, the K_c (demarcating the two level statistics) pushed towards lower K and at $g_\uparrow/g_\downarrow = 1$ the system exhibits Wigner-Dyson statistics. (b) Evolution of $\langle r\rangle$ as a function of W for three system sizes at $K = 1$ and $g_\uparrow/g_\downarrow = 0.2$. At lower W, the ergodic phase of the system (with complex eigenenergies) follows Ginibre ensemble statistics and at strong W, the MBL follows real Poisson statistics. The average value of $-\cos(\theta)$ as a function of (c) the interchain couplings at $W = 2$ and (d) disorder strengths for $K = 1$ and $g_\uparrow/g_\downarrow = 0.2$. The system size is $L = 8$, on-site interaction $U = 1$, and disorder average is performed for 100 realizations.

We first consider the evolution of $\langle r\rangle$ as a function of K for weak disorder ($W = 2$) [Fig. 3(a)]. For smaller K and $g_\uparrow \neq g_\downarrow$, the $\langle r\rangle$ attains a constant value ≈0.74, which corresponds to the Ginibre ensemble [61]. When K increases to the strong coupling limit ($K \gg 1$), Fig. 3(a) shows a transition to $\langle r\rangle \approx 0.56$ for the GOE distribution [65]. This transition is consistent with the corresponding complex-real transition of the eigenspectrum shown in Fig. 1(b). In Fig. 3(a) it is evident that the K_c, which demarcates Ginibre and GOE statistics, lowers as the ratio $g_\uparrow/g_\downarrow$ approaches unity. For $g_\uparrow/g_\downarrow = 1$, the $\langle r\rangle$ remains nearly GOE, because the non-Hermiticity can be removed by the imaginary gauge transformation under OBC. It is interesting to note that for $g_\uparrow/g_\downarrow = 1$, the correlated (spin-independent) disorder potential leads to a Poisson level distribution due to inherent SU(2) spin symmetry. Therefore, to have GOE statistics, we need an uncorrelated disorder potential which breaks the spin symmetry (see Appendix B for details).

Figure 3(b) shows $\langle r\rangle$ as a function of the disorder strength W for weak interchain coupling ($K = 1$). We demonstrate that the disorder-induced complex-real transition is accompanied by a change in $\langle r\rangle$ from Ginibre to real Poisson statistics. It is important to stress that the present non-Hermitian model has $\langle r\rangle \approx 0.5$ for the real Poisson statistics, which is different from the conventional $\langle r\rangle \approx 0.38$ of Hermitian many-body systems [63,64], even with both being characterized for real spectra. This fact is consistent with a recent study which characterizes the spacing ratio for the spectra of non-Hermitian random matrices [65]. Furthermore, the critical disorder strength of the transition $W_c \approx 9$ can be obtained by inspecting the crossing of $\langle r \rangle$ curves for the two largest systems. Combining Figs. 3(a) and 3(b), we note that for strong interchain coupling or $g_\uparrow/g_\downarrow = 1$, the disorder leads to a transition from GOE to Poisson distribution. Thus, at strong W, the effects of the disorder potential prevail and $\langle r \rangle$ value reaches a stationary value of the real Poisson statistics.

Likewise, the single-number signature of $\langle -\cos(\theta) \rangle$ distinguishes the ergodic and localized phases [61]. In Figs. 3(c) and 3(d) we show the evolution of the disorder-averaged $\langle -\cos(\theta) \rangle$ with K and W, respectively. We first consider $\langle -\cos(\theta) \rangle$ as a function of K for weak disorder [Fig. 3(c)]. At small K, we numerically find $\langle -\cos(\theta) \rangle \approx 0.22$ that corresponds to the Ginibre level distribution. This value is consistent with the analysis for the single Hatano-Nelson chain [61]. As K increases, we find a dip in $\langle -\cos(\theta) \rangle$ which demarcates the complex- and real-energy phases. Moreover, for larger $g_\uparrow/g_\downarrow$ (with $g_\uparrow \neq g_\downarrow$) the dip occurs at smaller K. On the other hand, for $g_\uparrow/g_\downarrow = 1$ the distribution of $\langle -\cos(\theta) \rangle$ does not change sign. The main features of $\langle -\cos(\theta) \rangle$ are in consonance with the eigenspectrum transition and evolution of $\langle r \rangle$. In Fig. 3(d) we further show the variation of $\langle -\cos(\theta) \rangle$ as a function of W for $K = 1$ and $g_\uparrow/g_\downarrow = 0.2$. As W increases, the value of $\langle -\cos(\theta) \rangle$ decreases, becomes negative, and eventually reaches $\langle -\cos(\theta) \rangle = 0$ for the Poisson statistics at strong disorder. This again confirms the disorder-induced spectral and localization transition.

C. Inverse participation ratio

To further understand the interplay between localization and NHSE in real space, we characterize the wave functions by employing the inverse participation ratio (IPR) and fractal dimension (FD). For non-Hermitian systems, the IPR can be defined in two ways: one using nth left or right eigenstates and other is defined under a biorthogonal basis from both left and right eigenstates. These are defined as

$$I_{n,s} = \frac{\sum_{i,\sigma} \left|\psi^n_{i,\sigma}\right|^2}{\left(\sum_{i,\sigma} \left|\psi^n_{i,\sigma}\right|\right)^2}, \quad I_{nB,s} = \frac{\sum_{i,\sigma} \left|\tilde{\psi}^n_{i,\sigma}\right|^2}{\left(\sum_{i,\sigma} \left|\tilde{\psi}^n_{i,\sigma}\right|\right)^2}, \tag{7}$$

where s is the disorder realization, the subscript nB represents the biorthogonal IPR, $\psi^n_{i,\sigma} \equiv (\langle n|b_{i,\sigma}\rangle^*)\langle n|b_{i,\sigma}\rangle$ and $\tilde{\psi}^n_{i,\sigma} \equiv (\langle \tilde{n}|b_{i,\sigma}\rangle^*)\langle n|b_{i,\sigma}\rangle$ with n and $\tilde{n}$ the right and corresponding left eigenstates, and $|b_{i,\sigma}\rangle$ are Fock space chosen as a computational basis. The IPRs are furthermore first averaged over numerous disorder realizations and then over the spectrum to get the mean IPRs, $I_{\text{avg}} = \sum_n \overline{I}_n/D$ and $I^B_{\text{avg}} = \sum_n \overline{I}_{nB}/D$ with D being the dimension of the Hilbert space and the overline denotes the disorder average. The disorder-averaged IPRs of eigenstate n are shown in Appendix C. For delocalized states, the IPR approaches zero in the thermodynamic limit while for localized states it saturates to a finite value ($\approx$1). The fractal dimension of an eigenstate is another measure which is recently devised to examine the localization properties of many-body systems [66,67]. The mean FD can be directly constructed from the mean IPRs as $\eta = -\ln(I_{\text{avg}})/\ln D$ and biorthogonal FD $\eta_B = -\ln(I^B_{\text{avg}})/\ln D$. The extended and localized phases are recognized by $\eta \to 1$ and $\eta \to 0$, respectively.

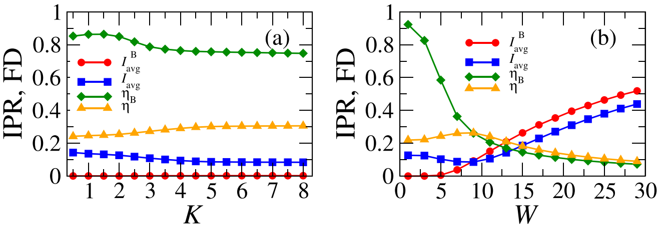

FIG. 4. Disorder-averaged IPR and FD of the right eigenstates (squares, triangles) and biorthogonal eigenstates (circles, diamonds) for the system size $L = 8$ and $g_\uparrow/g_\downarrow = 0.5$ at (a) $W = 2$ and (b) $K = 1$. Here the disorder average is performed for 100 samples.

In Fig. 4(a) we show the mean IPR and FD (defined in both ways) for open chains as a function of K for $W = 2$. It is interesting to note that the value of I_{avg} is nonzero even at weak disorder, whereas I^B_{avg} is zero. This suggests that the finite I_{avg} is due to the NHSE which plays a significant role at weak disorder, where the biorthogonal density distributions do not suffer from the NHSE. This fact can be understood from the similarity transformation $|n'\rangle = S^{-1}|n\rangle$ and $\langle n'| = \langle \tilde{n}|S$, with $|n'\rangle$ being the eigenstate of the corresponding Hermitian system. Hence, the biorthogonal density distributions are devoid of the NHSE. It is important to note that the choice of eigenstates for IPR is only important for open chains as under PBC the NHSE is absent. Furthermore, the corresponding contrast behavior in η and η_B is also noted, cf. Fig. 4(a). The evolution of I^B_{avg} and η_B with K confirms the delocalization at $W = 2$. While the system possesses a complex-real spectral transition with increase in K, as shown in Fig. 1(b), this transition does not overlap with the localization transition.

We further present the evolution of mean IPR and FD with W in Fig. 4(b). At lower W, the I^B_{avg} is small but I_{avg} acquires a finite value due to the interference of the NHSE. The η_B approaches unity at lower W representing the delocalization. The value of mean IPR (FD) increases (decreases) with W, confirms the disorder-driven localization in the non-Hermitian two-chain model. The observed behaviors of IPR and FD show that the disorder-driven localization transition overlaps to the complex-real spectral transition. In addition, we note that in contrast to the weak-disorder regime where a significant difference between η and η_B exists, at strong disorder the values predicted by η and η_B coincide. This indicates the suppression of NHSE in the presence of strong disorder strength. The finite-size effects of IPR are discussed in Appendix C.

D. Dynamical properties

Here we study the nonequilibrium time dynamics of the non-Hermitian system from the perspective of quantum trajectories with no-jump condition for the continuously measured system [15,68]. By choosing an arbitrary initial state $|\psi_0\rangle$ at $t = 0$, the time dynamics is encoded in the wave function

$$|\psi_t\rangle = \frac{e^{-i\mathcal{H}t/\hbar}\,|\psi_0\rangle}{\sqrt{\langle\psi_0|\,e^{i\mathcal{H}^\dagger t/\hbar}e^{-i\mathcal{H}t/\hbar}\,|\psi_0\rangle}}, \tag{8}$$

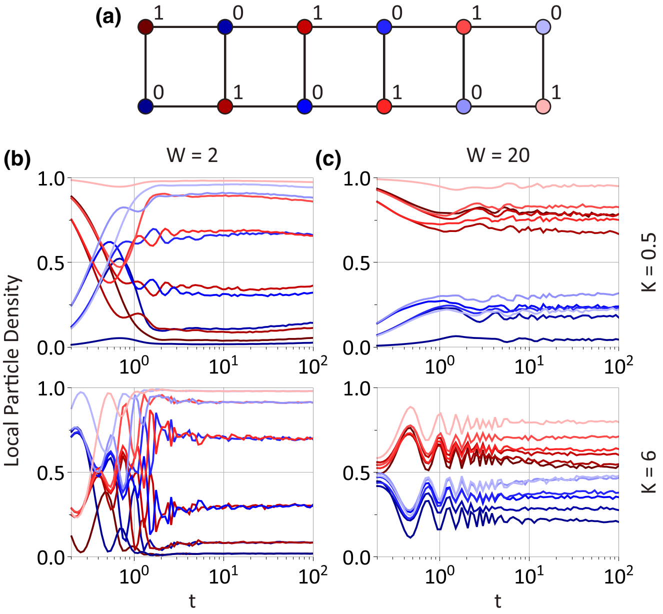

FIG. 5. (a) Schematic of the initial state $\hat{c}^\dagger_{1,\uparrow}\hat{c}^\dagger_{2,\downarrow}\hat{c}^\dagger_{3,\uparrow}\hat{c}^\dagger_{4,\downarrow}\cdots|\text{vac}\rangle$. The red (blue) dots are initially occupied (unoccupied) sites, and the dark to light gradients denote the spatial position from left to right. (b) and (c) The time evolution of the local particle density at each site for weak ($K = 0.5$, upper panel) and strong ($K = 6$, lower panel) interchain couplings. The dynamics at weak ($W = 2$) and strong ($W = 20$) disorder strengths are shown in (b) and (c), respectively. The plots are obtained by averaging over 500 disorder realizations, and the other parameters are $U = 1$ and $g_\uparrow/g_\downarrow = 0.5$.

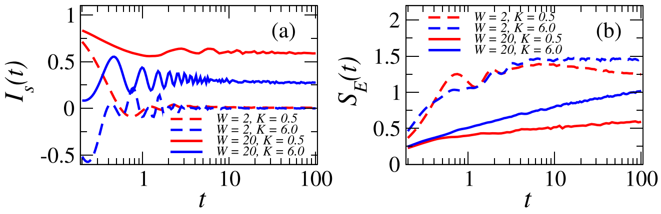

FIG. 6. The time dynamics of (a) spin imbalance and (b) bipartite entanglement entropy for $W = 2$ (dashed line) and $W = 20$ (solid line) at $K = 0.5$ (red) and $K = 6$ (blue). At $W = 20$, a nonvanishing stationary value of $I_s(t)$ and the logarithmic growth of $S_E(t)$ characterize the MBL. At weak disorder, the long-time dynamics of the entanglement entropy exhibits the decrease in the complex-energy phase ($K = 0.5$) while it remains steady in the real-energy phase ($K = 6$). The disorder average is performed over 500 realizations. Here the on-site interaction strength $U = 1$ and $g_\uparrow/g_\downarrow = 0.5$.

which is governed solely by the non-Hermitian effective Hamiltonian $\mathcal{H}$. With this time-dependent wave function, all the dynamical properties can be explored.

We first discuss the dynamics of the local particle density $n_{j,\sigma}(t)$ and spin imbalance $I_s(t)$ for different interchain couplings K and disorder strengths W. Here the spin imbalance is defined as

$$I_s(t) = \frac{1}{L}\sum_{j=1}^{L}(-1)^{j-1}[n_{j,\uparrow}(t) - n_{j,\downarrow}(t)], \qquad (9)$$

whose long-time stationary value effectively serves as an order parameter of many-body localized phase. We choose the Néel ordered state $|\uparrow\downarrow\uparrow\downarrow\cdots\rangle$ as an initial state, whose schematic representation is shown in Fig. 5(a). This state has $I_s(0) = 1$ at initial time ($t = 0$).

At weak disorder ($W = 2$), the time evolution of the local particle density for both small and strong interchain couplings are shown in Fig. 5(b). We observe that the saturation values of the local particle densities for $|\uparrow\rangle$ and $|\downarrow\rangle$ coincide at the same spatial indices. Thus, the corresponding $I_s(t)$ in Fig. 6(a) relaxes to zero as time evolves, losing memory of initial ordering, suggests delocalization of the system. On the other hand, Fig. 5(c) for strong disorder ($W = 20$) shows that the stationary values of the particles densities for $|\uparrow\rangle$ and $|\downarrow\rangle$ do not coincide at the same spatial indices, which leads to a nonvanishing steady value of $I_s(t)$ at long times in Fig. 6(a). This initial-state memory retention indicates the disorder-driven MBL. In addition, we find that at strong disorder, larger K suppresses the steady value of $I_s(t)$. This is because the K term couples different spin sectors and scrambles the initial spin ordering. Therefore, as the interchain coupling K increases, the disorder-driven localization transition occurs at higher W.

It is interesting to note that although the system is extended in character at weak disorder, the larger local particle density appears at the site closer to the right end of the chain [Fig. 5(b)]. This anomalous localization stems from the nonreciprocal tunnelings. However, we stress that this localization is suppressed by strong disorder in the MBL phase [Fig. 5(c)]. It is worth mentioning that the suppression of the NHSE-induced localization at strong disorder is also observed in the eigenstate properties, as discussed in Sec. III C.

We further investigate the dynamics of a half-chain von Neumann entanglement entropy which is defined as

$$S_E(t) = -\overline{\text{Tr}[\rho_A(t)\ln\rho_A(t)]}, \qquad (10)$$

where the two subsystems are denoted as A and B with $\rho_A(t) = \text{Tr}_B[|\psi_t\rangle\langle\psi_t|]$ being the reduced density matrix of subsystem A. Here Tr_B is the trace over degrees of freedom of subsystem B. The time evolution of $S_E(t)$ for various limits of K and W is shown in Fig. 6(b). For strong disorder strength we find the long-time evolution of $S_E(t)$ exhibits a logarithmic growth, which is reminiscent of nonergodicity in the Hermitian many-body localization [69,70]. For weak disorder, however, $S_E(t)$ can decrease after $t \approx 5$ in the complex eigenenergy phase ($K = 0.5$), but remain steady in the real eigenenergy one ($K = 6$). This long-time behavior of $S_E(t)$ signifies the real-complex transition unique to open non-Hermitian chains.

E. Experimental realization

The spectral and localization transitions reported in the present work can be qualitatively realized in a two-chain fermionic lattice with asymmetric hoppings. Recently it has been proposed that such nonreciprocal hopping can be effectively implemented by reservoir engineering [71–73]. It is worth mentioning that the implementation of a single Hatano-Nelson chain in cold-atom experiments has already been proposed [4]. Using a similar strategy in the implementation of two-component fermionic systems (such as a non-Hermitian Su-Schrieffer-Heeger model or two-chain system considered here) and allowing a Rabi-coupling K is feasible for cold atoms trapped in optical lattices [74–79]. The model Hamiltonian of the present work can be mapped to an effective non-Hermitian dissipative model. In particular, the Hamiltonian Eq. (1) can be rewritten into Hermitian $\hat{H}_1 = (\hat{H} + \hat{H}^\dagger)/2$ and anti-Hermitian $\hat{H}_2 = (\hat{H} - \hat{H}^\dagger)/2$ parts

$$\begin{aligned}\hat{H}_1 = {} & -\frac{J(e^{g_\sigma} + e^{-g_\sigma})}{2}\sum_{j,\sigma}(\hat{c}^\dagger_{j+1,\sigma}\hat{c}_{j,\sigma} + \hat{c}^\dagger_{j,\sigma}\hat{c}_{j+1,\sigma}) \\ & - \sum_j K(\hat{c}^\dagger_{j,\uparrow}\hat{c}_{j,\downarrow} + \hat{c}^\dagger_{j,\downarrow}\hat{c}_{j,\uparrow}) \\ & + U\sum_j \hat{n}_{j,\uparrow}\hat{n}_{j,\downarrow} + \sum_{j,\sigma}\epsilon_{j\sigma}\hat{n}_{j,\sigma}, \qquad (11a)\end{aligned}$$

$$\hat{H}_2 = -\frac{J(e^{g_\sigma} - e^{-g_\sigma})}{2}\sum_{j,\sigma}(\hat{c}^\dagger_{j+1,\sigma}\hat{c}_{j,\sigma} - \hat{c}^\dagger_{j,\sigma}\hat{c}_{j+1,\sigma}). \qquad (11b)$$

The Hermitian part of the Hamiltonian $\hat{H}_1$ in Eq. (11) with a random disorder potential can be constructed by superimposing an optical speckle field onto an optical lattice [80,81]. The disorder strength is proportional to the speckle field strength and therefore can be tuned. Moreover, with current advancement of ultracold atom experiments, it is possible to generate a spin-dependent disorder potential by using laser beams of different polarizations. The on-site interaction strength is tunable by adjusting the s-wave scattering length between two fermionic components using a Feshbach resonance [82]. Note that the implementation of a two-leg ladder system in a clean system is already performed in recent experiments [83–87], where the interchain tunneling of atoms can be controlled by the Raman transitions between the states.

The anti-Hermitian part $\hat{H}_2$ can be implemented by considering the jump operator that includes a collective one-body loss [4]

$$\hat{L}_{j,\sigma} = \sqrt{J\,|e^{g_\sigma} - e^{-g_\sigma}|}[\hat{c}_{j,\sigma} + i\,\mathrm{sgn}(g_\sigma)\hat{c}_{j+1,\sigma}], \qquad (12)$$

where $\mathrm{sgn}(g_\sigma)$ indicates the sign of g_σ and controls the direction of nonreciprocal tunnelings. Under no-jump condition or post-selection [15,68], the dynamics of the density matrix is solely governed by the following effective non-Hermitian Hamiltonian:

$$\begin{aligned}\hat{H}_{\mathrm{eff}} &= \hat{H}_1 - \frac{i}{2}\sum_\sigma\sum_{j=0}^{L}\hat{L}^\dagger_{j,\sigma}\hat{L}_{j,\sigma} \\ &= \hat{H}_1 + \hat{H}_2 - i\sum_\sigma\sum_{j=1}^{L} J\,|\sinh g_\sigma|\hat{c}^\dagger_{j,\sigma}\hat{c}_{j,\sigma}, \qquad (13)\end{aligned}$$

where the last term represents the on-site atom decay and we have considered the open boundary conditions at $j = 0$ with $\hat{L}_{0,\sigma} = \sqrt{J|e^{g_\sigma} - e^{-g_\sigma}|}i\mathrm{sgn}(g_\sigma)\hat{c}_{1,\sigma}$ and $j = L$ with $\hat{L}_{L,\sigma} = \sqrt{J\,|e^{g_\sigma} - e^{-g_\sigma}|}\hat{c}_{L,\sigma}$. It is evident that two chains have different decay terms at $g_\uparrow \neq g_\downarrow$. To compensate for this discrepancy, two chains should couple to different reservoirs to have the same on-site decay rate. In this case, the final effective non-Hermitian Hamiltonian differs from our model Hamiltonian in Eq. (1) by an overall decay term. Nevertheless, it would not affect the dynamics of the system as long as the no-jump condition holds, or the post-selection is considered, where the wave function is given by Eq. (8). In experiments such novel nonlocal loss can be engineered by nonlocal Rabi coupling as recently proposed in Ref. [4]. A nonreciprocal hopping effectively creates imaginary gauge fields and induces a non-Hermitian Aharonov-Bohm effect. More recently, the unique signatures of NHSE in many-body systems are observed [11], the implementation of a random disorder potential in such experimental settings could be a possible step towards realization of the model of the present study. We believe our results are within reach of current experimental progress and techniques.

IV. CONCLUSIONS

We discussed the eigenspectrum, level statistics, and localization properties of two coupled non-Hermitian chains. We unveiled the occurrence of two complex-real spectral transitions. One transition is induced by the interplay of nonreciprocal hoppings and interchain coupling which is absent under periodic boundary conditions, while the other one is driven by a random disorder potential and present under both open and periodic boundaries. Furthermore, we have studied both spectral transitions using level statistics, inverse participation ratio, and fractal dimension. We have shown the suppression of the non-Hermitian skin effect in the many-body localized phase. Finally, the time evolution of the local particle density, spin imbalance, and entanglement entropy corroborates the pivotal role of boundaries and characterizes the many-body localization. We believe the characteristics and results of our coupled-chain model are timely and pertinent, and can be readily implemented in various non-Hermitian systems. Our findings pave a way to further investigate the interplay of the boundary conditions, the disorder-driven localization, and the many-body dynamics in other non-Hermitian systems.

ACKNOWLEDGMENTS

We acknowledge the support of High Performance Computing Cluster at IAMS, Academia Sinica. K.S. acknowledges the support by Academia Sinica. This research has been supported by the Ministry of Science and Technology (MOST), Taiwan, under Grants No. MOST-109-2112-M-001-035-MY3 (Y.-C.W. and H.H.J.), No. MOST-110-2112-M-003-008-MY3 (Y.-C.W. and J.-S.Y.), and No. MOST-111-2636-M-007-009 (Y.-P.H.). Y.-P.H., H.H.J., and J.-S.Y. are also grateful for support from National Center for Theoretical Sciences in Taiwan.

APPENDIX A: FINITE-SIZE EFFECTS OF COMPLEX-ENERGY FRACTION AND ROLE OF BOUNDARY CONDITIONS

The eigenenergies of the model Hamiltonian [Eq. (1)] for $L = 8$ under OBC are shown in Figs. 7(a)–7(f). Since the system respects time-reversal symmetry and belongs to the symmetry class AI, the complex spectrum is symmetric with respect to the real axis. With the increase in K [Figs. 7(a)–7(c)] and W [Figs. 7(d)–7(f)], the imaginary parts of the energies are suppressed. The complex-real transition exists

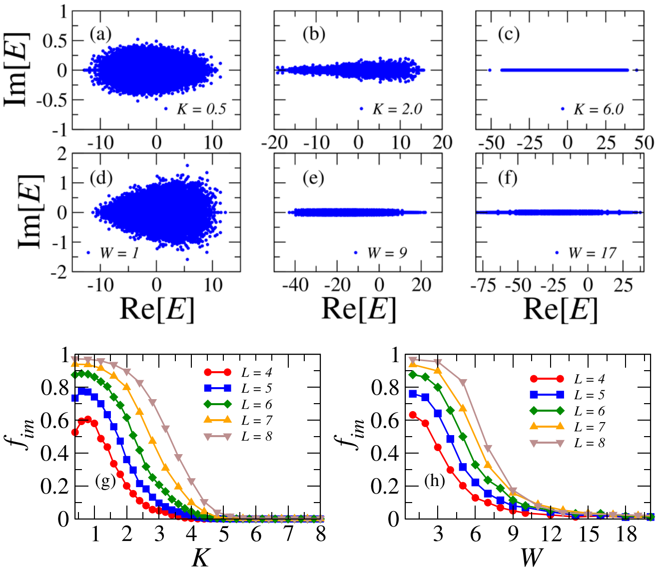

FIG. 7. Eigenenergies of the non-Hermitian coupled Hatano-Nelson open chains for $L = 8$ as a function of (a)–(c) the interchain coupling K at $W = 2$ and (d)–(f) the disorder strength W at $K = 1$. These are shown corresponding to Figs. 2(a)–2(f) of the main text. The decrease in the fraction of complex energies with K and W are evident. (g) and (h) The disorder-averaged complex energy fraction $f_{\rm im}$ as a function of (g) K and (h) W for different system sizes and $g_\uparrow/g_\downarrow = 0.2$.

for $g_\uparrow \neq g_\downarrow$ in a coupled non-Hermitian chains. For $g_\uparrow = g_\downarrow$, however, the spectrum remains real, because the imaginary gauge transformation is valid for this special case.

We present the finite-size effects on the complex energy fraction $f_{\rm im}$. Our analysis is restricted to the system size amenable to the exact diagonalization. We estimate the finite-size effects by comparison of $f_{\rm im}$ for smaller system sizes. We first discuss the interchain coupling driven spectral transition under OBC at weak disorder. The evolution of $f_{\rm im}$ with K at $g_\uparrow/g_\downarrow = 0.2$ and $W = 2$ for different system sizes are shown in Fig. 7(g). While the eigenenergies of a single Hatano-Nelson open chain are real, an infinitesimal coupling K between the chains with $g_\uparrow \neq g_\downarrow$ leads to complex energies. In this analysis we have varied the value of K from a small ($K = 0.3$) to a strong ($K = 8$) coupling limit. As seen from Fig. 7(g), the $f_{\rm im}$ shifts to a larger value as L increases, and at $L = 8$ the fraction of the complex energies $f_{\rm im} \approx 1$. This suggests the stability of the complex energy phase in the thermodynamic limit for small K. On the other hand, at strong interchain coupling, the $f_{\rm im}$ converges to zero as L increases. This shows the robustness of the spectral transitions shown in Fig. 1(b) of the main text. We believe the qualitative features of the spectral transitions holds in the thermodynamic limit, however the critical interchain coupling strength K_c might vary for larger system sizes.

We further discuss the finite-size effects on the spectral transition due to the disorder potential. The $f_{\rm im}$ for different system sizes as a function of W is shown in Fig. 7(h). Here we consider $K = 1$ and $g_\uparrow/g_\downarrow = 0.2$. For the considered parameters, at weak disorder strengths, the system possesses complex energies and remains in the delocalized phase. As disorder strength increases, we find a complex-real spectral transition beyond a critical value of W. It is important to note that a similar transition also appears in a single Hatano-Nelson chain under PBC [15]. Note that a single-chain under OBC does not possess such transition because of the real spectrum at weak disorder due to NHSE. Here, in the considered two-chain model, the transition occurs under OBC due to the interplay of K and g_σ's. At weak W, the $f_{\rm im}$ converges to unity as system size increases and with increases in W the $f_{\rm im}$ approaches zero signifying the complex-real transition. This confirms that the real spectrum at strong W shown in Fig. 1(c) is robust to change in L. Since the system sizes considered in the present work are small and the extrapolation to an infinite system size is difficult, hence we refrain from extracting the critical disorder strength W_c using a finite-size scaling approach. It is noteworthy that a similar argument also holds for a Hermitian MBL system where an asymmetric scaling is predicted to govern the localization transition [66,88–91]. Considering the subtleties of finite-size scaling near MBL transition, here we tentatively identify the W_c of the localization transition by the crossing of $f_{\rm im}$ curves for the largest system sizes available. This lead to $W_c \approx 9$ (see the crossing of curves for $L = 7$ and $L = 8$) at $K = 1$ and $g_\uparrow/g_\downarrow = 0.2$, which is consistent with the similar analysis done using a complex level-spacing ratio in the main text [Fig. 3(b)].

We now discuss the role of boundary conditions in terms of the model parameters K and W. The disorder-averaged $f_{\rm im}$ for $L = 6$ is shown in Fig. 8. For larger system sizes, the qualitative behavior of the energies does not change, however the critical value of the transitions might vary.

Under OBC, as discussed previously (and in the main text), the complex-real spectral transition induced by interchain coupling or by disorder is evident in Figs. 8(a)–8(c). For open coupled chains with unequal non-Hermiticity parameters or for hybridized chains ($g_\uparrow = 0, g_\downarrow \neq 0$ and vice-versa) the system possesses complex energies. While the system remains delocalized at $W = 2$, it exhibits the complex-real transition due to the interplay of non-Hermiticity and interchain coupling. Hence, we predict an eigenspectral transition, which does not coincide with the localization transition. As the $g_\uparrow/g_\downarrow$ approaches unity, the fraction of complex energies decreases and at $g_\uparrow = g_\downarrow$ the system exhibits real spectrum and is devoid of dynamical instability. For periodic chains, the eigenspectrum remains complex as a function of K at weak disorder, as illustrated in Figs. 8(d)–8(f). The complex nature of the energies with PBC is related to the plane-wave character of the eigenwave function and the prevailing role of nonreciprocal tunnelings. At strong disorder, the wave functions are localized (as ascertain by the eigenstate properties in the main text), and delocalization-localization transition coincides with the complex-real transition. In short, the K-driven transition is absent in the PBC case, whereas the W-driven is present for both boundary cases.

APPENDIX B: LEVEL DISTRIBUTIONS FOR $g_\uparrow = g_\downarrow$

For $g_\uparrow = g_\downarrow$, the IGT maps the non-Hermitian coupled-chain system to a Hermitian one [60]. In the meanwhile, the spectral properties strongly depend on the symmetries of disorder potential. The correlated (spin-independent)

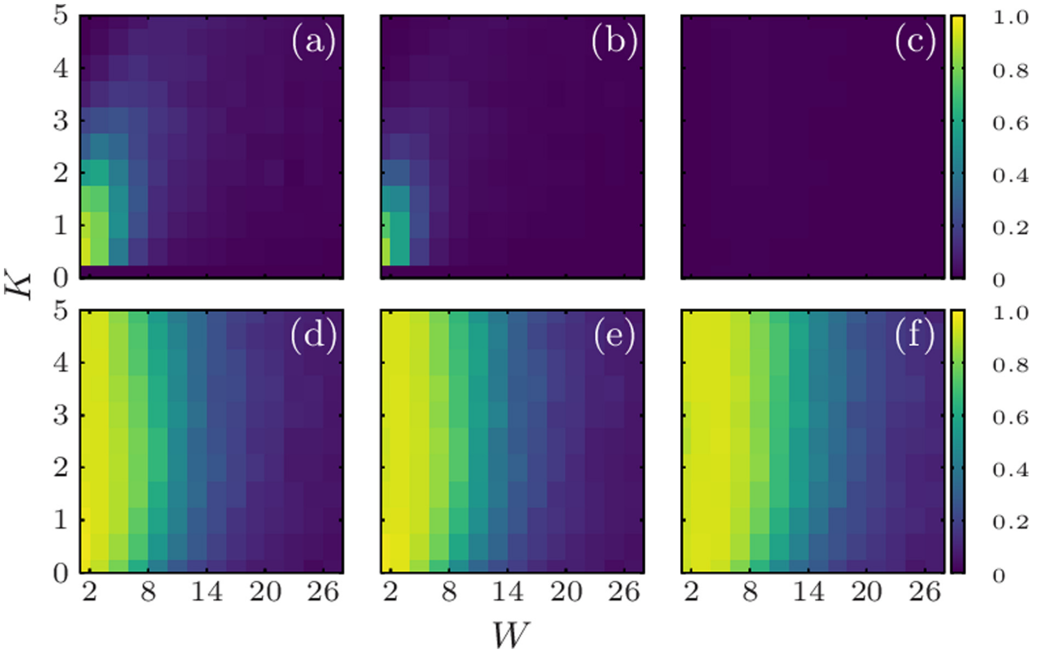

FIG. 8. The disorder-averaged f_{im} of open coupled chains are shown for (a) $g_\uparrow/g_\downarrow = 0.2$, (b) $g_\uparrow/g_\downarrow = 0.6$, and (c) $g_\uparrow/g_\downarrow = 1.0$. For the same values, the disorder-averaged f_{im} under PBC are shown in the lower panel (d)–(f). Under OBC, the $g_\uparrow/g_\downarrow = 1.0$ case (c) can be gauged out using IGT and hence the spectrum remains real in the entire K-W plane. For an open non-Hermitian coupled-chain system, the interchain coupling also drives the system into real eigenspectrum. Here the eigenspectrum is averaged over 500 disorder realizations.

disorder preserves SU(2) spin symmetry and leads to a Poisson level-spacing distribution at a delocalized regime. For the Hermitian disordered systems, it has been shown that a symmetry breaking field or diagonalization of a single symmetry block of the Hamiltonian leads to GOE-like behavior at weak disorder strength [56,92]. The uncorrelated (spin-dependent) potential breaks the spin symmetries and results into a GOE distribution. The nearest-neighbor level-spacing distributions for $W = 2$ and $g_\uparrow = g_\downarrow$ using two different disorder potentials are illustrated in Fig. 9.

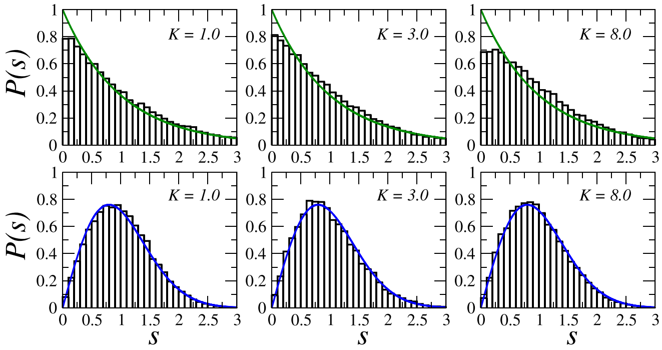

FIG. 9. The nearest-neighbor level-spacing distributions as a function of the interchain coupling strength K for $g_\uparrow = g_\downarrow$. The upper (lower) panel represents the distributions with correlated (uncorrelated) disorder for the system size $L = 8$. Here the disorder strength $W = 2$ and the distributions are averaged over 100 disorder realization. The green and blue lines represent the (real) Poisson and GOE level-spacing distributions, respectively.

APPENDIX C: FINITE-SIZE EFFECTS OF INVERSE PARTICIPATION RATIO

Here we discuss the disorder-averaged inverse participation ratio as a function of the eigenstate index. As discussed in the main text, for the non-Hermitian systems, the IPR can be defined in two ways: $\bar{I}_n$ is defined using nth left or right eigenstate while $\bar{I}_{nB}$ is using the biorthogonal basis. Here the overline denotes the disorder average. Figure 10(a) shows $\bar{I}_{nB}$ and $\bar{I}_n$ in the whole energy spectrum. The

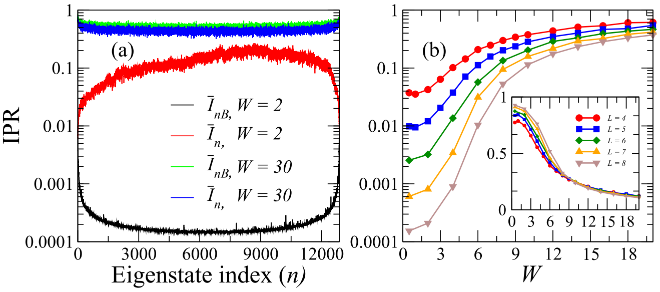

FIG. 10. (a) The disorder-averaged inverse participation ratio obtained using nth right eigenstates ($\bar{I}_n$) and biorthogonal IPR ($\bar{I}_{nB}$) for open coupled chains of $L = 8$. The averaged IPR is shown for two disorder strengths: one in the delocalized ($W = 2$) and other in the localized ($W = 30$) regime. The other parameters of the model are $K = 1$ and $g_\uparrow/g_\downarrow = 0.5$. (b) The finite-size effects of biorthogonal IPR (averaged over both disorder realizations and Hilbert space) as a function of the disorder strength (W). At weak W, the IPR approaches zero in the delocalized regime and at strong W, the IPR of different system sizes converges to one. In the inset of (b) we show the corresponding biorthogonal fractal dimension for different L.

parameters considered are $K = 1$, $g_\uparrow/g_\downarrow = 0.5$, and $L = 8$. At weak disorder ($W = 2$), IPR is small, suggesting delocalization. Interestingly, the IPR $\bar{I}_n$ shows a finite value while $\bar{I}_{nB} \approx 0$ for $W = 2$. As explained in the main text, the finite $\bar{I}_n$ at weak disorder can be attributed to the presence of NHSE. At strong W, the large values of IPR suggest many-body localization. Furthermore, both definitions of IPR give similar values, indicating the suppression of NHSE at strong disorder. It is important to note that the choice of eigenstates for IPR is only important for open chains. Under PBC, the results from both definitions coincide due to the absence of NHSE. We next present the finite-size effects on biorthogonal IPR and corresponding fractal dimension in Fig. 10(b). Here we consider the biorthogonal definitions so that the interference of NHSE-induced phenomena can be eliminated and we could inspect system-size effects on the role of disorder potential. At weak disorder strengths, the averaged-IPR decreases with an increase in L. The contrast behavior is also seen for biorthogonal fractal dimension. Hence, at weak disorder $I^B_{\text{avg}} \to 0$ (or $\eta_B \to 1$) with an increase in L, indicating the delocalized regime. As W increases, the IPR tends to approach unity, and converse behavior of FD is evident from the inset in Fig. 10(b). The convergence in IPR and FD for different system sizes confirms the disorder-driven many-body localization of non-Hermitian coupled chains.

[1] C. M. Bender and S. Boettcher, Phys. Rev. Lett. **80**, 5243 (1998).
[2] S. Longhi, Phys. Rev. Lett. **103**, 123601 (2009).
[3] Y. Ashida, S. Furukawa, and M. Ueda, Nat. Commun. **8**, 15791 (2017).
[4] Z. Gong, Y. Ashida, K. Kawabata, K. Takasan, S. Higashikawa, and M. Ueda, Phys. Rev. X **8**, 031079 (2018).
[5] Y. Ashida, Z. Gong, and M. Ueda, Adv. Phys. **69**, 249 (2020).
[6] E. J. Bergholtz, J. C. Budich, and F. K. Kunst, Rev. Mod. Phys. **93**, 015005 (2021).
[7] L. Xiao, T. Deng, K. Wang, G. Zhu, Z. Wang, W. Yi, and P. Xue, Nat. Phys. **16**, 761 (2020).
[8] T. Helbig, T. Hofmann, S. Imhof, M. Abdelghany, T. Kiessling, L. W. Molenkamp, C. H. Lee, A. Szameit, M. Greiter, and R. Thomale, Nat. Phys. **16**, 747 (2020).
[9] T. Hofmann, T. Helbig, F. Schindler, N. Salgo, M. Brzezińska, M. Greiter, T. Kiessling, D. Wolf, A. Vollhardt, A. Kabaši, C. H. Lee, A. Bilušić, R. Thomale, and T. Neupert, Phys. Rev. Research **2**, 023265 (2020).
[10] W. Gou, T. Chen, D. Xie, T. Xiao, T.-S. Deng, B. Gadway, W. Yi, and B. Yan, Phys. Rev. Lett. **124**, 070402 (2020).
[11] Q. Liang, D. Xie, Z. Dong, H. Li, H. Li, B. Gadway, W. Yi, and B. Yan, Phys. Rev. Lett. **129**, 070401 (2022).
[12] N. Hatano and D. R. Nelson, Phys. Rev. Lett. **77**, 570 (1996).
[13] N. Hatano and D. R. Nelson, Phys. Rev. B **56**, 8651 (1997).
[14] N. Hatano and D. R. Nelson, Phys. Rev. B **58**, 8384 (1998).
[15] R. Hamazaki, K. Kawabata, and M. Ueda, Phys. Rev. Lett. **123**, 090603 (2019).
[16] L.-J. Zhai, S. Yin, and G.-Y. Huang, Phys. Rev. B **102**, 064206 (2020).
[17] T. Orito and K.-I. Imura, Phys. Rev. B **105**, 024303 (2022).
[18] J. Ginibre, J. Math. Phys. **6**, 440 (1965).
[19] R. Grobe, F. Haake, and H.-J. Sommers, Phys. Rev. Lett. **61**, 1899 (1988).
[20] F. Haake, *Quantum Signatures of Chaos* (Springer, Berlin, 2013).
[21] S. Yao and Z. Wang, Phys. Rev. Lett. **121**, 086803 (2018).
[22] V. M. Martinez Alvarez, J. E. Barrios Vargas, and L. E. F. Foa Torres, Phys. Rev. B **97**, 121401(R) (2018).
[23] D. S. Borgnia, A. J. Kruchkov, and R.-J. Slager, Phys. Rev. Lett. **124**, 056802 (2020).
[24] N. Okuma, K. Kawabata, K. Shiozaki, and M. Sato, Phys. Rev. Lett. **124**, 086801 (2020).
[25] K. Zhang, Z. Yang, and C. Fang, Phys. Rev. Lett. **125**, 126402 (2020).
[26] T. Yoshida, T. Mizoguchi, and Y. Hatsugai, Phys. Rev. Research **2**, 022062(R) (2020).
[27] K. Kawabata, M. Sato, and K. Shiozaki, Phys. Rev. B **102**, 205118 (2020).
[28] R. Okugawa, R. Takahashi, and K. Yokomizo, Phys. Rev. B **102**, 241202(R) (2020).
[29] Y. Fu, J. Hu, and S. Wan, Phys. Rev. B **103**, 045420 (2021).
[30] K. Zhang, Z. Yang, and C. Fang, Nat. Commun. **13**, 2496 (2022).
[31] Y.-C. Wang, J.-S. You, and H. H. Jen, Nat. Commun. **13**, 4598 (2022).
[32] K. Yokomizo and S. Murakami, Phys. Rev. Lett. **123**, 066404 (2019).
[33] S. Weidemann, M. Kremer, T. Helbig, T. Hofmann, A. Stegmaier, M. Greiter, R. Thomale, and A. Szameit, Science **368**, 311 (2020).
[34] S. Liu, R. Shao, S. Ma, L. Zhang, O. You, H. Wu, Y. J. Xiang, T. J. Cui, and S. Zhang, Research **2021**, 5608038 (2021).
[35] M. Brandenbourger, X. Locsin, E. Lerner, and C. Coulais, Nat. Commun. **10**, 4608 (2019).
[36] A. Ghatak, M. Brandenbourger, J. van Wezel, and C. Coulais, Proc. Natl. Acad. Sci. USA **117**, 29561 (2020).
[37] E. Lee, H. Lee, and B.-J. Yang, Phys. Rev. B **101**, 121109(R) (2020).
[38] S. Mu, C. H. Lee, L. Li, and J. Gong, Phys. Rev. B **102**, 081115(R) (2020).
[39] T. Yoshida, Phys. Rev. B **103**, 125145 (2021).
[40] W. Zhang, F. Di, H. Yuan, H. Wang, X. Zheng, L. He1, H. Sun, and X. Zhang, Phys. Rev. B **105**, 195131 (2022).
[41] T. Liu, J. J. He, T. Yoshida, Z.-L. Xiang, and F. Nori, Phys. Rev. B **102**, 235151 (2020).
[42] K. Cao, Q. Du, X.-R. Wang, and S.-P. Kou, arXiv:2109.03690.
[43] D.-W. Zhang, Y.-L. Chen, G.-Q. Zhang, L.-J. Lang, Z. Li, and S.-L. Zhu, Phys. Rev. B **101**, 235150 (2020).
[44] Z. Xu and S. Chen, Phys. Rev. B **102**, 035153 (2020).
[45] F. Alsallom, L. Herviou, O. V. Yazyev, and M. Brzezińska, Phys. Rev. Research **4**, 033122 (2022).

[46] S.-B. Zhang, M. M. Denner, T. Bzdušek, M. A. Sentef, and T. Neupert, arXiv:2201.12653.

[47] K. Kawabata, K. Shiozaki, and S. Ryu, Phys. Rev. B **105**, 165137 (2022).

[48] L. Li, C. H. Lee, S. Mu, and J. Gong, Nat. Commun. **11**, 5491 (2020).

[49] L. Li, C. H. Lee, and J. Gong, Commun. Phys. **4**, 42 (2021).

[50] K. Yokomizo and S. Murakami, Phys. Rev. B **104**, 165117 (2021).

[51] S. Mu, L. Zhou, L. Li, and J. Gong, Phys. Rev. B **105**, 205402 (2022).

[52] S. M. Rafi-Ul-Islam, Z. B. Siu, H. Sahin, C. H. Lee, and M. B. A. Jalil, Phys. Rev. Research **4**, 013243 (2022).

[53] G. Lemut, M. Mierzejewski, and J. Bonča, Phys. Rev. Lett. **119**, 246601 (2017).

[54] M. Środa, P. Prelovšek, and M. Mierzejewski, Phys. Rev. B **99**, 121110(R) (2019).

[55] B. Leipner-Johns and R. Wortis, Phys. Rev. B **100**, 125132 (2019).

[56] K. Suthar, P. Sierant, and J. Zakrzewski, Phys. Rev. B **101**, 134203 (2020).

[57] R. Hamazaki, K. Kawabata, N. Kura, and M. Ueda, Phys. Rev. Research **2**, 023286 (2020).

[58] K. Kawabata, K. Shiozaki, M. Ueda, and M. Sato, Phys. Rev. X **9**, 041015 (2019).

[59] H. Zhou and J. Y. Lee, Phys. Rev. B **99**, 235112 (2019).

[60] N. Hatano and H. Obuse, Ann. Phys. **435**, 168615 (2021).

[61] L. Sá, P. Ribeiro, and T. Prosen, Phys. Rev. X **10**, 021019 (2020).

[62] H. Markum, R. Pullirsch, and T. Wettig, Phys. Rev. Lett. **83**, 484 (1999).

[63] V. Oganesyan and D. A. Huse, Phys. Rev. B **75**, 155111 (2007).

[64] Y. Y. Atas, E. Bogomolny, O. Giraud, and G. Roux, Phys. Rev. Lett. **110**, 084101 (2013).

[65] T. Peron, Bruno Messias F. de Resende, F. A. Rodrigues, L. F. Costa, and J. A. Méndez-Bermúdez, Phys. Rev. E **102**, 062305 (2020).

[66] N. Macé, F. Alet, and N. Laflorencie, Phys. Rev. Lett. **123**, 180601 (2019).

[67] A. Bäcker, M. Haque, and I. M. Khaymovich, Phys. Rev. E **100**, 032117 (2019).

[68] A. J. Daley, Adv. Phys. **63**, 77 (2014).

[69] M. Žnidarič, T. Prosen, and P. Prelovšek, Phys. Rev. B **77**, 064426 (2008).

[70] J. H. Bardarson, F. Pollmann, and J. E. Moore, Phys. Rev. Lett. **109**, 017202 (2012).

[71] J. F. Poyatos, J. I. Cirac, and P. Zoller, Phys. Rev. Lett. **77**, 4728 (1996).

[72] S. Diehl, A. Micheli, A. Kantian, B. Kraus, H. P. Büchler, and P. Zoller, Nat. Phys. **4**, 878 (2008).

[73] S. Diehl, E. Rico, M. A. Baranov, and P. Zoller, Nat. Phys. **7**, 971 (2011).

[74] J. Li, A. K. Harter, J. Liu, L. de Melo, Y. N. Joglekar, and L. Luo, Nat. Commun. **10**, 855 (2019).

[75] F. Song, S. Yao, and Z. Wang, Phys. Rev. Lett. **123**, 170401 (2019).

[76] S. Lapp, J. Ang'ong'a, F. A. An, and B. Gadway, New J. Phys. **21**, 045006 (2019).

[77] L. Li, C. H. Lee, and J. Gong, Phys. Rev. Lett. **124**, 250402 (2020).

[78] S. Longhi, Phys. Rev. Lett. **128**, 157601 (2022).

[79] Z. Ren, D. Liu, E. Zhao, C. He, K. K. Pak, J. Li, and G.-B. Jo, Nat. Phys. **18**, 385 (2022).

[80] M. Pasienski, D. McKay, M. White, and B. DeMarco, Nat. Phys. **6**, 677 (2010).

[81] J.-y. Choi, S. Hild, J. Zeiher, P. Schauß, A. Rubio-Abadal, T. Yefsah, V. Khemani, D. A. Huse, I. Bloch, and C. Gross, Science **352**, 1547 (2016).

[82] X.-W. Guan, M. T. Batchelor, and C. Lee, Rev. Mod. Phys. **85**, 1633 (2013).

[83] J. H. Kang, J. H. Han, and Y. Shin, Phys. Rev. Lett. **121**, 150403 (2018).

[84] J. H. Han, J. H. Kang, and Y. Shin, Phys. Rev. Lett. **122**, 065303 (2019).

[85] J. H. Kang, J. H. Han, and Y. Shin, New J. Phys. **22**, 013023 (2020).

[86] J. H. Han, D. Bae, and Y. Shin, Phys. Rev. A **105**, 043306 (2022).

[87] P. Lauria, W.-T. Kuo, N. R. Cooper, and J. T. Barreiro, Phys. Rev. Lett. **128**, 245301 (2022).

[88] I. García-Mata, J. Martin, R. Dubertrand, O. Giraud, B. Georgeot, and G. Lemarié, Phys. Rev. Research **2**, 012020(R) (2020).

[89] N. Laflorencie, G. Lemarié, and N. Macé, Phys. Rev. Research **2**, 042033(R) (2020).

[90] A. Morningstar, D. A. Huse, and J. Z. Imbrie, Phys. Rev. B **102**, 125134 (2020).

[91] D. Abanin, J. Bardarson, G. De Tomasi, S. Gopalakrishnan, V. Khemani, S. Parameswaran, F. Pollmann, A. Potter, M. Serbyn, and R. Vasseur, Ann. Phys. **427**, 168415 (2021).

[92] R. Mondaini and M. Rigol, Phys. Rev. A **92**, 041601(R) (2015).